

# Extremely large magnetoresistance and chiral anomaly in the nodal-line semimetal $\text{ZrAs}_2$

Junjian Mi,<sup>1,2</sup> Sheng Xu,<sup>1</sup> Shuxiang Li,<sup>1,2</sup> Chenxi Jiang,<sup>1,2</sup> Zheng Li,<sup>1,2</sup> Qian Tao,<sup>1</sup> and Zhu-An Xu<sup>1,2,3,4,\*</sup>

<sup>1</sup>*School of Physics, Zhejiang University, Hangzhou, 310058, China*

<sup>2</sup>*State Key Laboratory of Silicon and Advanced Semiconductor Materials, Zhejiang University, Hangzhou, 310027, China*

<sup>3</sup>*Hefei National Laboratory, Hefei, 230088, China*

<sup>4</sup>*Collaborative Innovation Centre of Advanced Microstructures, Nanjing University, Nanjing, 210093, China*

(Dated: March 3, 2025)

We performed the detailed magnetotransport measurements and first principle calculations to study the electronic properties of the transition metal dipnictides  $\text{ZrAs}_2$ , which is a topological nodal-line semimetal. Extremely large unsaturated magnetoresistance (MR) which is up to  $1.9 \times 10^4$  % at 2 K and 14 T was observed with magnetic field along the  $c$ -axis. The nonlinear magnetic field dependence of Hall resistivity indicates the multi-band features, and the electron and hole are nearly compensated according to the analysis of the two-band model, which may account for the extremely large unsaturated MR at low temperatures. The evident Shubnikov-de Haas (SdH) oscillations at low temperatures are observed and four distinct oscillation frequencies are extracted. The first principle calculations and angle-dependent SdH oscillations reveal that the Fermi surface consists of three pockets with different anisotropy. The observed twofold symmetry MR with electric field along the  $b$ -axis direction is consistent with our calculated Fermi surface structures. Furthermore, the negative magnetoresistance (NMR) with magnetic field in parallel with electric field is observed, which is an evident feature of the chiral anomaly.

## INTRODUCTION

The study of topological semimetals have attracted tremendous interests due to their novel electronic structure and unconventional transport properties in condensed-matter physics in recent years [1–3], such as large longitudinal magnetoresistance, high mobility, nontrivial Berry phase and chiral-anomaly induced negative longitudinal MR [4–10]. In these materials, the topological semimetallic states are characterized by band touching points or lines between conduction and valance bands in momentum space. Dirac and Weyl semimetals are characterized by band crossings at a single point in  $k$ -space, exhibiting linear dispersion and featuring fourfold and twofold degeneracies, respectively. Dirac points could be divided into two Weyl points by breaking time-reversal symmetry or inversion symmetry. Dirac semimetals have been confirmed in  $\text{Cd}_3\text{As}_2$  and  $\text{Na}_3\text{Bi}$  [11–14] and Weyl semimetals have been theoretically proposed and experimentally observed in  $\text{MX}$  ( $\text{M}=\text{Ta}$  or  $\text{Nb}$ ;  $\text{X}=\text{P}$  or  $\text{As}$ ),  $\text{WTe}_2$  and  $(\text{Nb,Ta})\text{IrTe}_4$  [15–21]. In contrast to Dirac or Weyl semimetals, topological nodal line semimetals showcase a unique characteristic: one-dimensional trajectory within the  $k$ -space, forming either an open path or a closed loop. Several candidate materials have been identified within the realm of nodal line semimetals, including  $\text{PbTaSe}_2$ ,  $\text{PtSn}_4$ ,  $\text{ZrSiX}$  ( $\text{X}=\text{S}$ ,  $\text{Se}$ ,  $\text{Te}$ ), and the  $\text{CaP}_3$  family ( $\text{A}=\text{Ca}$ ,  $\text{Ba}$ ,  $\text{Sr}$ ;  $\text{B}=\text{P}$ ,  $\text{As}$ ). Each of these materials exhibits intriguing topological properties [22–27].

The transition metal dipnictides (TMDPs) with the formula  $\text{MX}_2$  (where  $\text{M}=\text{Nb}$  or  $\text{Ta}$ ;  $\text{X}=\text{As}$  or  $\text{Sb}$ ) exhibit a crystalline structure characterized by the symmetry of  $C2/m$  (No. 12), and they have attracted considerable attention primarily owing to their possession of compelling properties, including extremely large magnetoresistance (XMR) and negative magnetoresistance (NMR) [9, 10, 28]. Recently, TMDPs  $\text{ZrX}_2$  (where  $\text{X}=\text{P}$  or  $\text{As}$ ) with the space group  $Pnma$  (No. 62) were

theoretically predicted to be topological nodal-line semimetals, garnering increasing attention. An extremely large magnetoresistance in  $\text{ZrP}_2$  has been detected, which might be induced by the compensation of electrons and holes. The compensation of electrons pockets and hole pockets were further confirmed by angle-resolved photoemission spectroscopy (ARPES) as well as the first-principle calculations [29, 30]. The band structure of  $\text{ZrP}_2$  is characterized by a nodal loop in the  $k_x = 0$  plane without considering spin-orbit coupling (SOC) and a small gap along the nodal loop will open when considering SOC according to the first-principle calculations [29]. Compared with  $\text{ZrP}_2$ , the gap of  $\text{ZrAs}_2$  along the node line should be larger due to the enhanced spin-orbit coupling [6].

Quantum oscillations, Hall resistivity, and anisotropic MR in  $\text{ZrAs}_2$  have recently been reported [31]. However, the topological properties have yet to be confirmed and the transport properties are worth revisiting with enhanced sample quality. Only one oscillation frequency (i.e., single pocket in Fermi surface) was observed from the SdH oscillations with the current applying along the  $b$ -axis and the magnetic field in the  $ac$  plane of  $\text{ZrAs}_2$ . In contrast, multiple pockets were detected in de Haas-van Alphen (dHvA) oscillations. Furthermore, recent ARPES experiments have reported the surface bands and bulk states of  $\text{ZrAs}_2$ , suggesting multi-band feature [32]. Such a discrepancy between transport and magnetic measurements could result from the low sample quality indicated by the lower residual resistivity ratio (RRR) of the previous samples grown by the flux method.

In this work, we reported the detailed magnetotransport properties and electronic structure of the topological nodal-line semimetal  $\text{ZrAs}_2$ . We used chemical vapor transport method to grow high quality crystals of  $\text{ZrAs}_2$  to investigate topological properties. The Hall resistivity and longitudinal MR measurements reveal the concentration of electron ( $n_e \approx$

$3.58 \times 10^{20} \text{cm}^{-3}$ ) with a mobility of  $\mu_e \approx 5600 \text{cm}^2 \text{V}^{-1} \text{s}^{-1}$  and the concentration of hole ( $n_h \approx 3.47 \times 10^{20} \text{cm}^{-3}$ ) with a mobility of  $\mu_h \approx 5164 \text{cm}^2 \text{V}^{-1} \text{s}^{-1}$  at 2 K, according to the analysis of the two-band model. The XMR up to  $1.9 \times 10^4$  % is observed at 2 K and 14 T, which is considered to stem from the compensation mechanism [29]. The SdH oscillations at low temperature and high magnetic field are observed and four frequencies  $F_1 = 155$  T,  $F_2 = 178$  T,  $F_3 = 443$  T,  $F_4 = 579$  T are extracted. The nontrivial Berry phases are obtained from the plot of the Landau level index fan diagram. Moreover, we observed anisotropic MR with two-fold symmetry when the current is applied along the  $b$  axis and the magnetic field lies within the  $ac$  plane, consistent with the two-fold Fermi surfaces (FSs) structure predicted by the DFT calculations. Furthermore, we observed the evident NMR when the electric field is in parallel with magnetic field applying along the  $b$  axis. According to our analysis and previous theoretical works[33], we argued that the NMR should be induced by the chiral anomaly. Our study has provided compelling evidence for the topological properties of nodal-line semimetals in  $\text{ZrAs}_2$ .

## EXPERIMENTAL METHODS

Single crystals of  $\text{ZrAs}_2$  were synthesized by the chemical vapor transport method. The Zr power and As power were weighted with a molar ratio of 1:2 in sealed fused-silica tubes with 4 mg/mL grain of  $\text{I}_2$  added to promote crystal growth. The quartz tubes were heated to  $850^\circ\text{C}$  over 2 days, kept at  $850^\circ\text{C}$  for 1 week and cooled to room temperature over 1 day, as described in Ref [34]. Then needle-like crystals were obtained. The atomic composition of the  $\text{ZrAs}_2$  single crystal was determined using energy dispersive X-ray spectroscopy (EDS), revealing a Zr to As ratio of 1:1.92. This observed ratio aligns closely with the nominal ratio of 1:2, taking into account experimental errors. A suitable crystal was selected and mounted on a Bruker D8 Venture diffractometer to measure the single crystal X-ray diffraction (XRD). The crystal was kept at 170.0 K during data collection. Using Olex2 [35], the structure was solved with the SHELXT [36] structure solution program using Intrinsic Phasing and refined with the SHELXL [37] refinement package using Least Squares minimisation.

The measurements of resistivity and magnetic transport properties were performed on a Quantum Design physical property measurement system (PPMS-DynaCool 14 T). The DFT calculations of electronic structure of bulk  $\text{ZrAs}_2$  were performed by using the Vienna ab initio simulation package (VASP) [38], with the generalized gradient approximation (GGA) in the Perdew-Burke-Ernzerhof type as the exchange-correlation energy [39]. The cutoff energy was set to 350 eV and  $\Gamma$ -centered  $8 \times 15 \times 6$  mesh were sampled over the Brillouin zone integration. The lattice constant  $a = 6.7964 \text{ \AA}$ ,  $b = 3.6848 \text{ \AA}$ ,  $c = 9.0214 \text{ \AA}$  was used for all the calculations. The tight-binding model of  $\text{ZrAs}_2$  was constructed by

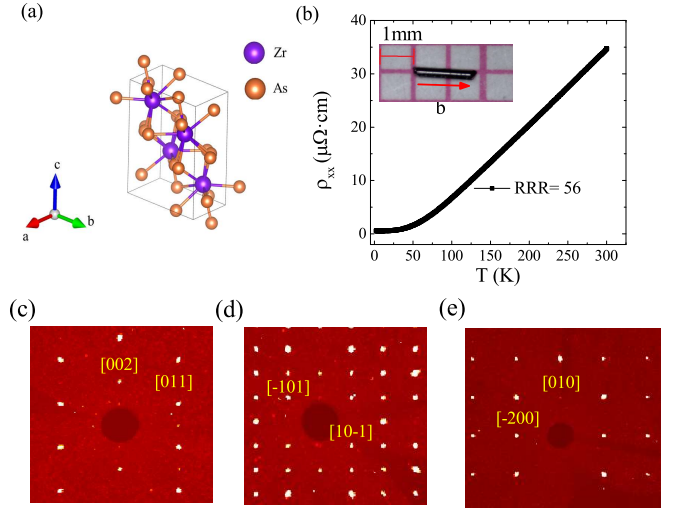


FIG. 1. (a) Crystalline structure of  $\text{ZrAs}_2$ . (b) Temperature-dependent resistivity of the single crystal  $\text{ZrAs}_2$ . The inset shows a photograph of the grown  $\text{ZrAs}_2$  single crystal. (c)-(e) Single-crystal XRD on  $\text{ZrAs}_2$  with Diffracted reflections in  $(0kl)$  plane,  $(h0l)$  plane  $(hk0)$  plane, respectively.

the Wannier90 with  $4d$  orbitals of Zr and  $4p$  orbitals of As, which based on the maximally-localized Wannier functions [40] [41].

## RESULTS AND DISCUSSIONS

The crystal structure of  $\text{ZrAs}_2$  is presented in Fig. 1(a) with the space group of  $Pnma$  (No. 62). Fig. 1(b) shows the temperature-dependent  $\rho_{xx}$  exhibiting a typical metallic behavior with the electric current along the  $b$ -axis. The residual resistivity  $\rho_{xx}(2\text{K})$  is  $0.53 \mu\Omega\text{-cm}$  at 2 K and residual resistance ratio ( $\text{RRR} = \rho_{xx}(300\text{K})/\rho_{xx}(2\text{K})$ ) is 56 which is higher than previously reported value in Ref. [31]. A higher  $\text{RRR}$  indicates a higher quality of single crystals. The inset shows a picture of the needle shaped single crystal  $\text{ZrAs}_2$  with the easy growth direction along the  $b$ -axis. Figs. 1(c-e) presents the diffracted reflections in  $(0kl)$  plane,  $(h0l)$  plane and  $(hk0)$  plane, respectively. The lattice constants of  $\text{ZrAs}_2$  were obtained as  $a = 6.7964(3) \text{ \AA}$ ,  $b = 3.6848(2) \text{ \AA}$ ,  $c = 9.0214(4) \text{ \AA}$ , which are consistent with the previous reported results [34].

Fig. 2(a) shows the field-dependent longitudinal MR of  $\text{ZrAs}_2$  at various temperatures, where MR is defined as  $\text{MR} = (\rho_{xx}(B) - \rho_{xx}(0))/\rho_{xx}(0) \times 100\%$ . To eliminate the Hall contribution, the  $\rho_{xx}(B)$  is calculated from  $\rho_{xx}(B) = (\rho_{xx}(-B) + \rho_{xx}(B))/2$ . An extremely large unsaturated MR of up to  $2.5 \times 10^3$  % is observed at 2 K and 8 T. The MR decreases as temperature increases, reaching  $1.6 \times 10^2$  % at 80 K and 8 T. To explore the origin of this large and unsaturated MR, we also measured the Hall resistivity. The measurements of  $\rho_{xy}(B)$  at different temperatures provide further transport features, as shown in Fig. 2(b). The Hall resistivity exhibits

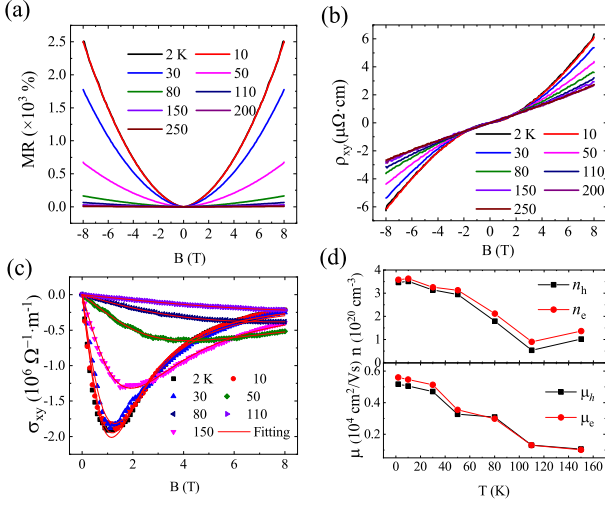


FIG. 2. (a) The longitudinal MR with the current along the  $b$  axis and magnetic field under the  $ac$  plane at various temperatures. (b) Hall resistivities versus magnetic field at different temperatures. (c)  $\sigma_{xy}$  versus magnetic field at different temperatures. The red curves are the fitting results by two-band model. (d) The temperature dependence of carrier densities and mobilities of the electrons and holes.

nonlinear magnetic field dependence at low temperatures, implying its multi-band properties. Furthermore, the mobility and concentration of electron and hole can be obtained by a two-band model fitting. Firstly, we calculated the  $\sigma_{xy}$  according to the formula  $\sigma_{xy} = -\rho_{xy}/((\rho_{xy})^2 + (\rho_{xx})^2)$ , then we fit the  $\sigma_{xy}$  using the two-band model formula as the following.

$$\sigma_{xy}(B) = \left( \frac{n_h \mu_h^2}{1 + (\mu_h B)^2} - \frac{n_e \mu_e^2}{1 + (\mu_e B)^2} \right) eB \quad (1)$$

where  $n_{e,h}$  and  $\mu_{e,h}$  represent the concentration and mobility of electrons and holes, respectively. As shown in Fig. 2(c), the fitted red curves are consistent with the experimental data, from which the temperature-dependent concentrations and mobilities are extracted and plotted in Fig. 2(d). At 2 K, the concentration of electron  $n_e \approx 3.58 \times 10^{20} \text{ cm}^{-3}$  which is almost equal to the concentration of hole  $n_h \approx 3.47 \times 10^{20} \text{ cm}^{-3}$ . The mobilities increase with decreasing temperature.  $\mu_e$  and  $\mu_h$  reach up to  $5600 \text{ cm}^2 \text{ V}^{-1} \text{ s}^{-1}$  and  $5164 \text{ cm}^2 \text{ V}^{-1} \text{ s}^{-1}$  at 2 K, respectively. The high mobilities further illustrate the good quality of single crystals. According to these results and analysis, the compensation mechanism of electrons and holes can account for the origin of the XMR at low temperature. Similarly, the compensation mechanism of electrons and holes induced XMR has been reported in other topological semimetals such as TaAs<sub>2</sub>, NbAs<sub>2</sub> and ZrP<sub>2</sub> [9, 10, 29].

Quantum oscillation experiments serve as a potent approach to investigate the properties of Fermi surfaces [42, 43]. Fig. 3(a) shows the resistivity as a function of magnetic field at low temperatures with the electric current along the  $b$ -axis and the magnetic field along the  $c$ -axis. The SdH oscillations

can be clearly observed at low temperatures and high magnetic fields. The inset shows obvious oscillations around 14 T. The oscillations gradually decrease as temperature increases and almost disappears at 12 K. The oscillatory components of the SdH oscillations versus  $1/B$  can be described by the Lifshitz-Kosevich (LK) formula [44–47]:

$$\Delta\rho \propto \frac{\lambda T}{\cosh(\lambda T)} e^{-\lambda T_D} \sin\left[2\pi\left(\frac{F}{B} - \frac{1}{2} + \beta + \delta\right)\right] \quad (2)$$

where  $\lambda = (2\pi^2 k_B m^*)/(\hbar e B)$ .  $T_D$  is the Dingle temperature. The value of  $\delta$  depends on the dimensionality,  $\delta = 0$  for 2D systems and  $\delta = \pm 1/8$  for 3D systems.  $\beta = \phi_B/2\pi$  and  $\phi_B$  is the Berry phase. After subtracting a background, the oscillation component  $\Delta\rho$  versus  $1/B$  is shown in Fig. 3(b). The oscillation intensity decreases with increasing temperature. Four oscillation frequencies can be identified from the Fast Fourier transform (FFT) analysis with  $F_1 = 155 \text{ T}$ ,  $F_2 = 178 \text{ T}$ ,  $F_3 = 443 \text{ T}$  and  $F_4 = 579 \text{ T}$  at low temperatures as shown in Fig. 2(c). Furthermore, the harmonic frequency  $2F_3 = 886 \text{ T}$  and  $2F_4 = 1158 \text{ T}$  can also be observed. Accord-

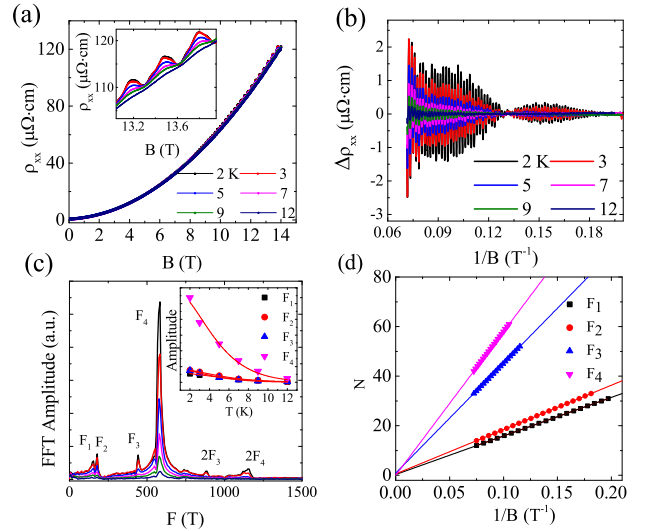


FIG. 3. (a) SdH oscillations at low temperatures with current along the  $b$ -axis and magnetic field along the  $c$ -axis. Inset: enlarged plot of SdH oscillations at high fields. (b) Oscillatory part of the resistivity  $\Delta\rho$  as a function of  $1/B$  at different temperatures. (c) FFT curves indicate the presence of four distinct intrinsic frequencies. Inset shows the temperature dependence of relative FFT amplitude of the frequencies as a function of temperature and the read curves are fitted by the thermal factor of Lifshitz-Kosevich formula. (d) Landau-level indices fan diagram for different frequencies as a function of  $1/B$ .

ing to the Onsager relation  $F = (\phi_0/2\pi^2) = (\hbar/2\pi e)A_F$ , the oscillation frequency is proportional to the extreme cross-section ( $A_F$ ) of FS normal to the magnetic field. The calculated  $A_F$  associated with different frequency were shown in Table 1. The inset of Fig. 3(c) shows the temperature-dependent FFT amplitudes and the red curve are fitted by the thermal factor  $R_T = (\lambda T)/\sinh(\lambda T)$ . The fitting curves are

consistent with experiment data and the effective masses are estimated to be  $m_1^* = 0.10m_e$ ,  $m_2^* = 0.11m_e$ ,  $m_3^* = 0.13m_e$  and  $m_4^* = 0.12m_e$ . The detailed fitting results are listed in Table 1. Compared to previous reports [31], we obtained lighter effective masses, which are corresponding to the Dirac fermions with linear dispersion. This suggests that the electronic properties of this material are more akin to ideal Dirac fermions. Besides, according to the Lifshitz - Onsager quantization rule  $N = A_F(\hbar/2\pi eB) - 1/2 + \beta + \delta$ , the Berry phase can be extracted from the intercept of the linear extrapolation. The Landau indices  $N$  as a function of  $1/B$  and the fitting curves are shown in Fig. 3(d). The values of  $\phi_B$  from the different  $\delta$  are listed in Table 1. The Berry phases of  $F_3$  with ( $\delta = 1/8$ ) is  $1.1\pi$  and  $F_4$  with ( $\delta = -1/8$ ) is  $0.8\pi$ , indicating the nontrivial  $\pi$  Berry phases. The nontrivial Berry phases indicate the topological properties of corresponding bands and FSs.

To further investigate the FS topology and compare it with results of the SdH experiments, we performed the DFT calculations. The FSs structures in the first Brillouin zone are displayed in Fig. 4(a)-4(c).  $\text{ZrAs}_2$  has small  $\alpha$  hole pockets (blue) near U point and two big  $\beta$  hole pockets as shown in Fig. 4(c) and Fig. 4(d) and three type  $\delta$  electron pockets (purple) near  $\Gamma$  point can be divided as  $\delta_1$  and  $\delta_2$ , which is similar to its sister compound  $\text{ZrP}_2$  [6]. In addition, there is also a small electron-like FS inside  $\delta_2$ . There are two additional small Fermi surfaces located inside the  $\delta_2$  Fermi surfaces. Moreover, both large Fermi surfaces,  $\beta$  and  $\delta_2$ , exhibit two-fold symmetry in the first Brillouin zone.

Angular-dependent magnetotransport measurements provide a valuable approach for investigating the detailed structure of the FS [43]. Fig. 4(d) shows the angle-dependent MR as a function of magnetic field at 2 K. The inset of Fig. 4(d) presents the definition of  $\varphi$  where the magnetic field is always perpendicular to the current. The evident SdH oscillations are observed when  $H$  rotates from the  $a$  axis to  $c$  axis. The angle-dependent  $\Delta\rho$  as a function of  $1/B$  at different angles are shown in Fig. 4(e). The intensities of oscillations increase with decreasing  $\varphi$  which is consistent with the tendency of MR. Fig. 4(f) shows the angle-dependent frequency of SdH oscillations as the rotation angle changes from the  $a$  axis ( $\varphi = 0^\circ$ ) to  $c$  axis ( $\varphi = 90^\circ$ ). As we mentioned hereinbefore, the four frequencies,  $F_1$ ,  $F_2$ ,  $F_3$  and  $F_4$ , appear as  $B//c$ . Due to the complicated FSs, we draw a red dash line in Fig. 4(f) to carefully track the position of these frequencies at different angles. The frequencies of  $F_1$  and  $F_2$  change slightly. However, the signals of  $F_1$  and  $F_2$  disappear at  $\varphi = 0^\circ$ , which possibly is obscured by the signal from a larger pocket. The frequencies of  $F_3$  increased with decreasing  $\varphi$ . However, the frequency of  $F_4$  increases first and then decreases with decreasing  $\varphi$ . The Fermi surfaces  $\beta$  and  $\delta_2$  in  $\text{ZrAs}_2$  are quite complex, which makes it difficult to distinguish the SdH oscillations of different FSs. The calculated frequencies of  $\delta_1$ ,  $\delta_2$  and  $\beta$  pockets are 135 T, 394 T and 551 T respectively, with magnetic field along the  $c$ -axis. The frequency  $F_1=155$  T may be associated with a small Fermi surface hidden within  $\delta_2$ . Combined with

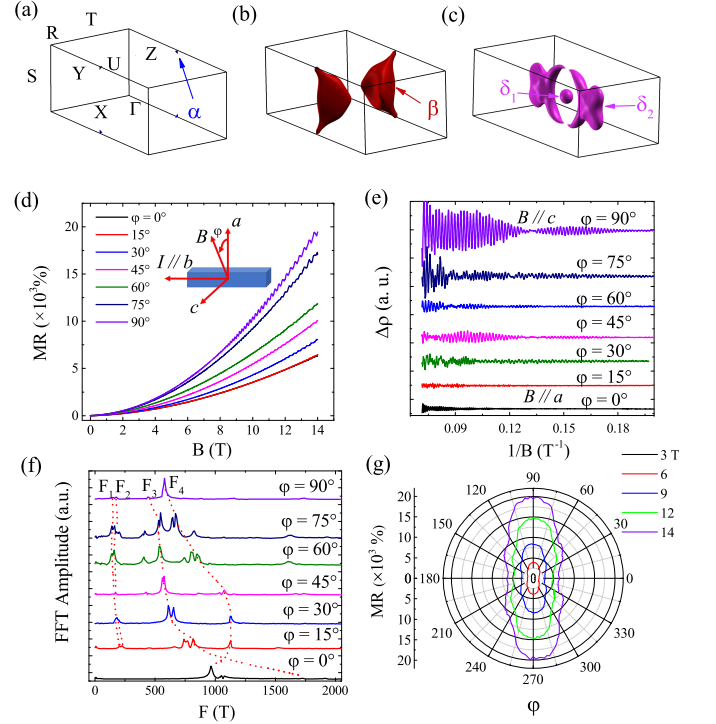


FIG. 4. (a) Brillouin zone and FSs of electron pockets (blue ones). (b) FSs of hole pockets (red ones). (c) FSs of electron pockets (purple ones). (d) Angle-dependent MR as a function of magnetic field of  $\text{ZrAs}_2$  by tilting the magnetic fields from  $B//a$  direction to the  $B//c$  direction with the current along the  $b$  direction at 2 K. (e) Angle-dependent  $\Delta\rho$  as a function of  $1/B$  at different angles. (f) Angle-dependent frequency from SdH oscillations at different angles. (g) Angle-dependent MR at different magnetic field by tilting the magnetic fields under the  $(ac)$  plane.

DFT calculations, we propose that  $F_2$  is associated with electron pocket  $\delta_1$ ,  $F_3$  is associated with electron pocket  $\delta_2$  and  $F_4$  is associated with hole pocket  $\beta$  as shown in Fig. 4(a) - 4(c). However, the oscillation frequency of small hole  $\alpha$  pocket is not observed in the SdH oscillations. The discrepancy between the SdH experiments and the DFT calculations may be induced by the slight variation in chemical potential of our sample. The chemical potential is often influenced by the small changes in the lattice parameters or impurity doping. In addition, the angle-dependent MR at 2 K is shown in Fig. 4(g) with current along the  $b$  axis and magnetic field in the  $ac$  plane. Besides, the obvious two-fold symmetry of MR were observed and the ratio of  $\rho_{xx}(14\text{T}, (\varphi = 90^\circ)) / \rho_{xx}(14\text{T}, (\varphi = 0^\circ)) \approx 3$  also indicates a moderate electronic structure anisotropy [43]. The twofold FSs can account for the two-fold symmetry anisotropic MR [48]. At 2 K and 14 T, the extremely large unsaturated MR reaches up to  $1.9 \times 10^4\%$  with magnetic field applied along the  $c$  axis, which is significantly higher than that of  $1.01 \times 10^3\%$  in previous report [31], indicating higher quality of the single crystals.

In addition to the non-trivial Berry phase identified through quantum oscillation analysis, a compelling piece of evidence

TABLE I. The parameters extracted from SdH oscillations with  $B \perp c$ -axis configuration. The  $F_1$ ,  $F_2$ ,  $F_3$  and  $F_4$  are the FSs from SdH oscillations;  $m^*/m_e$  is the ratio of the effective mass to the electron mass;  $\phi_B$  is the Berry phase.

Pocket	Frequency(T)	$A_F(\text{\AA}^{-2})$	$\phi_B(\delta = -1/8)$	$\phi_B(\delta = 1/8)$	$m^*/m_e$
$F_1$	155	0.015	$1.4\pi$	$0.9\pi$	0.10
$F_2$	178	0.017	$1.9\pi$	$0.4\pi$	0.11
$F_3$	443	0.042	$0.6\pi$	$1.1\pi$	0.13
$F_4$	579	0.055	$0.8\pi$	$1.3\pi$	0.12

for the topological characteristics is the observation of chiral anomaly induced negative MR (NMR), which have been observed in Weyl semimetal NbAs and Dirac semimetal TaAs<sub>2</sub> and NbAs<sub>2</sub> [9, 10]. Fig. 5(a) shows the angle-dependent longitudinal MR at 2 K with magnetic field rotating from perpendicular to in parallel with current ( $I//b$ ). In order to eliminate the influence of the Hall signal, the  $\rho_{xx}(B)$  were averaged by measuring the resistivity over positive and negative field directions. At  $\theta = 0^\circ$ , the MR is the largest. As  $\theta$  decreases, the MR at 2 K decreases dramatically under magnetic field. When magnetic field is collinear with current ( $\theta = 0^\circ$ ), the chiral anomaly plays a significant role in the transport. As shown in Fig. 5(b), when the magnetic field is parallel to current ( $B//I$ ), a clear negative MR is observed. When the magnetic field increases, the MR becomes positive at low fields ( $B < 5$  T) and negative at high fields below 50K, at  $\theta = 90^\circ$ . It should be noted that such a NMR was not in Ref. [31]. Similar NMR induced by the chiral anomaly has widely observed in topological semimetals like NbAs<sub>2</sub> in Ref. [9]. According to the theoretical works and related experiments[5, 26, 33], when magnetic field is collinear with electric field in the topological nodal line semimetal, a chiral anomaly will appear remarkably which is similar to the Weyl semimetal. The chiral anomaly can account for the NMR when the magnetic field is collinear with the electric field ( $B//I$ ), which indicates again the topological characteristic of ZrAs<sub>2</sub>.

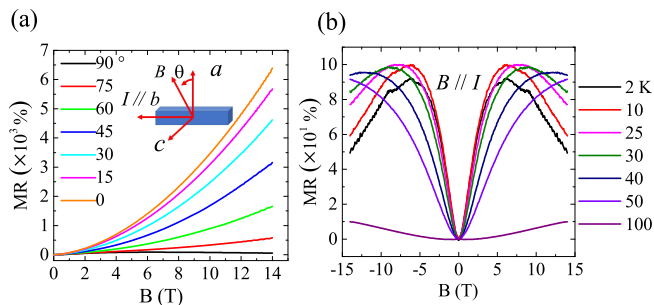


FIG. 5. (a) Angle-dependent MR as a function of magnetic field of ZrAs<sub>2</sub> by titling the magnetic fields from the a direction ( $B \perp I$ ) to the  $B // I$  direction at 2 K. (b) Magnetic field-dependent MR at different temperatures with  $B//I$  along the b-axis direction.

Besides the chiral anomaly, there may be other mechanisms that can also give rise to negative MR. Firstly, our ZrAs<sub>2</sub> sample is high quality single crystalline which should not contain

any magnetic atoms, thus the influence of magnetic moments can be excluded. Secondly, Anderson weak antilocalization (WAL) can also cause negative MR at low fields [49]. However, as shown in Fig. 5(b), the negative MR in our case appears in high magnetic field ( $B > 5$  T), therefore the WAL effect could be excluded. Thirdly, the NMR can also be induced in the quantum limit, where the Fermi energy lies in the only the lowest Landau level [50, 51]. In our case, the quantum oscillations can be observed at high magnetic field as shown in Fig. 2(a), the influence of quantum limit can be excluded. Finally, the current jetting effect can induce NMR when inhomogeneous currents are injected into the sample. To mitigate this, we positioned the current injection electrodes across the sample to ensure a uniform current distribution throughout the sample, thereby avoiding the influence of the current jetting effect [5]. To summarize, based on above discussions, and also considering theoretical calculations and analysis, we argued that the NMR in ZrAs<sub>2</sub> should be induced by the chiral anomaly.

## CONCLUSIONS

In summary, the detailed magnetotransport properties and electron structures of topological nodal-line semimetal ZrAs<sub>2</sub> were measured. The extremely large unsaturated MR is observed which reaches up to  $1.9 \times 10^4$  % at 2 K and 14 T. The electron- and hole-type charge carriers are almost compensated from the analysis based on the two-band model, which may account for the extremely large unsaturated MR at low temperature. The evident SdH oscillations are observed and four frequencies  $F_1 = 155$  T,  $F_2 = 178$  T,  $F_3 = 443$  T and  $F_4 = 579$  T are extracted from the SdH oscillations. The nontrivial  $\pi$  Berry phase and the chiral anomaly induced NMR suggested its nontrivial topological characteristic. Our study further confirmed the topological characteristics of nodal-line semimetal ZrAs<sub>2</sub>.

## ACKNOWLEDGMENTS

This work was supported by the National Science Foundation of China (Grant No. 12174334; 12204410), the National Key & Program of the China (Grant No. 2019YFA0308602), the Innovation Program for Quantum Science and Technology (Grant No. 2021ZD0302500), and China Postdoctoral Science Foundation (Grant No. 2022M712788)

- \* zhuan@zju.edu.cn
- [1] C.-K. Chiu, J. C. Y. Teo, A. P. Schnyder, and S. Ryu, *Rev. Mod. Phys.* 88, 035005 (2016).
- [2] N. P. Armitage, E. J. Mele, and A. Vishwanath, *Rev. Mod. Phys.* 90, 015001 (2018).
- [3] B. Yan and C. Felser, *Annu. Rev. Condens. Matter Phys.* 8, 337 (2017).
- [4] N. Kumar, Y. Sun, N. Xu, K. Manna, M. Yao, V. Süss, I. Leermakers, O. Young, T. Förster, M. Schmidt, H. Borrmann, B. Yan, U. Zeitler, M. Shi, C. Felser, and C. Shekhar, *Nat. Commun.* 8, 1642 (2017).
- [5] L. An, X. Zhu, W. Gao, M. Wu, W. Ning, and M. Tian, *Phys. Rev. B* 99, 045143 (2019).
- [6] J. Bannies, E. Razzoli, M. Michiardi, H.-H. Kung, I. S. Elfimov, M. Yao, A. Fedorov, J. Fink, C. Jozwiak, A. Bostwick, E. Rotenberg, A. Damascelli, and C. Felser, *Phys. Rev. B* 103, 155144 (2021).
- [7] D. T. Son and B. Z. Spivak, *Phys. Rev. B* 88, 104412 (2013).
- [8] Y. Luo, H. Li, Y. Dai, H. Miao, Y. Shi, H. Ding, A. Taylor, D. Yarotski, R. Prasankumar, and J. Thompson, *Appl. Phys. Lett.* 107, 182411 (2015).
- [9] B. Shen, X. Y. Deng, G. Kotliar, and N. Ni, *Phys. Rev. B* 93, 195119 (2016).
- [10] Y.-Y. Wang, Q.-H. Yu, P.-J. Guo, K. Liu, and T.-L. Xia, *Phys. Rev. B* 94, 041103(R) (2016).
- [11] S. M. Young, S. Zaheer, J. C. Y. Teo, C. L. Kane, E. J. Mele, and A. M. Rappe, *Phys. Rev. Lett.* 108, 140405 (2012).
- [12] Z. Wang, H. Weng, Q. Wu, X. Dai, and Z. Fang, *Phys. Rev. B* 88, 125427 (2013).
- [13] Z. K. Liu, B. Zhou, Y. Zhang, Z. J. Wang, H. M. Weng, D. Prabhakaran, S.-K. Mo, Z. X. Shen, Z. Fang, X. Dai, Z. Hussain, and Y. L. Chen, *Science* 343, 864 (2014).
- [14] S. Borisenko, Q. Gibson, D. Evtushinsky, V. Zabolotnyy, B. Büchner, and R. J. Cava, *Phys. Rev. Lett.* 113, 027603 (2014).
- [15] S.-Y. Xu, N. Alidoust, I. Belopolski, Z. Yuan, G. Bian, T.-R. Chang, H. Zheng, V. N. Strocov, D. S. Sanchez, G. Chang, C. Zhang, D. Mou, Y. Wu, L. Huang, C.-C. Lee, S.-M. Huang, B. Wang, A. Bansil, H.-T. Jeng, and T. Neupert et al., *Nat. Phys.* 11, 748 (2015).
- [16] S.-Y. Xu, I. Belopolski, N. Alidoust, M. Neupane, G. Bian, C. Zhang, R. Sankar, G. Chang, Z. Yuan, C.-C. Lee, S.-M. Huang, H. Zheng, J. Ma, D. S. Sanchez, B. Wang, A. Bansil, F. Chou, P. P. Shibayev, H. Lin, and S. Jia et al., *Science* 349, 613 (2015).
- [17] P. Li, Y. Wen, X. He, Q. Zhang, C. Xia, Z.-M. Yu, S. A. Yang, Z. Zhu, H. N. Alshareef, and X.-X. Zhang, *Nat. Commun.* 8, 2150 (2017).
- [18] B. Q. Lv, H. M. Weng, B. B. Fu, X. P. Wang, H. Miao, J. Ma, P. Richard, X. C. Huang, L. X. Zhao, G. F. Chen, Z. Fang, X. Dai, T. Qian, and H. Ding, *Phys. Rev. X* 5, 031013 (2015).
- [19] C. Shekhar, A. K. Nayak, Y. Sun, M. Schmidt, M. Nicklas, I. Leermakers, U. Zeitler, Y. Skourski, J. Wosnitza, Z. Liu, Y. Chen, W. Schnelle, H. Borrmann, Y. Grin, C. Felser, and B. Yan, *Nat. Phys.* 11, 645 (2015).
- [20] B. Q. Lv, S. Muff, T. Qian, Z. D. Song, S. M. Nie, N. Xu, P. Richard, C. E. Matt, N. C. Plumb, L. X. Zhao, G. F. Chen, Z. Fang, X. Dai, J. H. Dil, J. Mesot, M. Shi, H. M. Weng, and H. Ding, *Phys. Rev. Lett.* 115, 217601 (2015).
- [21] X. W. Huang, X. X. Liu, P. Yu, P. L. Li, J. Cui, J. Yi, J. B. Deng, J. Fan, Z. Q. Ji, F. M. Qu, X. N. Jing, C. L. Yang, L. Lu, Z. Liu, and G. T. Liu, *Chin. Phys. Lett.* 36, 077101 (2019).
- [22] L. M. Schoop, M. N. Ali, C. Straßer, A. Topp, A. Varykhalov, D. Marchenko, V. Duppel, S. S. P. Parkin, B. V. Lotsch, and C. R. Ast, *Nat. Commun.* 7, 11696 (2016).
- [23] Y. Wu, L.-L. Wang, D. Mun, D. D. Johnson, D. Mou, L. Huang, Y. Lee, S. L. Bud'ko, P. C. Canfield, and A. Kaminski, *Nat. Phys.* 12, 667 (2016).
- [24] J. Hu, Z. J. Tang, J. Y. Liu, X. Liu, Y. L. Zhu, D. Graf, K. Myhro, S. Tran, C. N. Lau, and J. Wei et al., *Phys. Rev. Lett.* 117, 016602 (2016).
- [25] J. Hu, Z. Tang, J. Liu, Y. Zhu, J. Wei, and Z. Mao, *Phys. Rev. B* 96, 045127 (2017).
- [26] Q. Xu, R. Yu, Z. Fang, X. Dai, and H. Weng, *Phys. Rev. B* 95, 045136 (2017).
- [27] G. Bian, T.-R. Chang, R. Sankar, S.-Y. Xu, H. Zheng, T. Neupert, C.-K. Chiu, S.-M. Huang, G. Chang, I. Belopolski, D. S. Sanchez, M. Neupane, N. Alidoust, C. Liu, B. Wang, C.-C. Lee, H.-T. Jeng, C. Zhang, Z. Yuan, and S. Jia et al., *Nat. Commun.* 7, 10556 (2016).
- [28] X.-T. Zhou, C.-H. Hsu, H. Aramberri, M. Iraola C.- Y. Huang, J.- L. Mañes, M.G. Vergniory, H. Lin, and N.Kioussis *Phys. Rev. B* 104, 125135 (2021).
- [29] K. Wang, D. Graf, L. Li, L. Wang, and C. Petrovic, *Anisotropic giant magnetoresistance in NbSb<sub>2</sub>*, *Sci. Rep.* 4, 7328 (2014).
- [30] J. Bannies, E. Razzoli, M. Michiardi, H.-H. Kung, I. S. Elfimov, M. Yao, A. Fedorov, J. Fink, C. Jozwiak, A. Bostwick, E. Rotenberg, A. Damascelli, and C. Felser, *Phys. Rev. B* 103, 155144 (2021).
- [31] S. Nandi, B. B. Maity, V. Sharma, R. Verma, V. Saini, B. Singh, D. Aoki, and A. Thamizhavel, *Phys. Rev. B* 109, 075155 (2024).
- [32] A. S. Wadge, K. Zborecki, B. J. Kowalski, D. Jastrzebski, P. K. Tanwar, P. Iwanowski, R. Diduszko, A. Moosarikandy, M. Rosmus, N. Olszowska, and A. Wisniewski, *Phys. Rev. B* 110, 035142 (2024).
- [33] S. Li, Z. Guo, D. Fu, X.-C. Pan, J. Wang, K. Ran, S. Bao, Z. Ma, Z. Cai, R. Wang, R. Yu, J. Sun, F. Song, and J. Wen, *Sci. Bull.* 63, 535 (2018).
- [34] P. E. Blanchard, R. G. Cavell, and A. Mar, *J. Alloys Compd.* 505, 17 (2010).
- [35] Dolomanov, O.V., Bourhis, L.J., Gildea, R.J, Howard, J.A.K. and Puschmann, H. (2009), *J. Appl. Cryst.* 42, 339-341.
- [36] Sheldrick, G.M. (2015). *Acta Cryst.* A71, 3-8.
- [37] Sheldrick, G.M. (2015). *Acta Cryst.* C71, 3-8.
- [38] G. Kresse and J. Furthmuller, *Phys. Rev. B* 54, 11169 (1996).
- [39] J. P. Perdew, K. Burke, and M. Ernzerhof, *Phys. Rev. Lett.* 77, 3865 (1996).
- [40] A. A. Mostofi, J. R. Yates, G. Pizzi, Y.-S. Lee, I. Souza, D. Vanderbilt, and N. Marzari, *Comput. Phys. Commun.* 185, 2309 (2014).
- [41] A. Kokalj, *J. Mol. Graphics Modell.* 17, 176 (1999).
- [42] Y. P. Li, C. C. Xu, M. S. Shen, J. H. Wang, X. H. Yang, X. J. Yang, Z. W. Zhu, C. Cao, and Z. A. Xu, *Phys. Rev. B* 98, 115145 (2018).
- [43] Y.-Y. Wang, P.-J. Guo, S. Xu, K. Liu, and T.- L. Xia, *Phys. Rev. B* 101, 035145 (2020).
- [44] I. M. Lifshits and A. M. Kosevich, *Sov. Phys. JETP* 2, 636 (1956).
- [45] D. Shoenberg, (Cambridge University Press, Cambridge, 1984).
- [46] I. Lifshitz, *Zh. Eksp. Teor. Fiz.* 38, 1569 (1960).
- [47] I. Lifshitz et al., *Sov. Phys. JETP* 11, 1130 (1960).
- [48] S. Zhang, Q. Wu, Y. Liu, and O. V. Yazyev *Phys. Rev. B* 99, 035142 (2019).

- [49] X. S. Wu, X. B. Li, Z. M. Song, C. Berger, and W. A. de Heer, Phys. Rev. Lett. 98, 136801 (2007).
- [50] P. Goswami, J. H. Pixley, and S. Das Sarma, Phys. Rev. B 92, 075205 (2015).
- [51] P. N. Argyres and E. N. Adams, Phys. Rev. 104, 900 (1956).